Sensitivity of quantitative vibrational coherent anti-Stokes Raman spectroscopy to saturation and Stark shifts

M. Péalat, M. Lefebvre, and J.-P. E. Taran
Office National d'Etudes et de Recherches Aérospatiales, Boite Postale 72, 92322 Châtillon Cédex, France

P. L. Kelley
Lincoln Laboratory, Massachusetts Institute of Technology, Lexington, Massachusetts 02173-0073
(Received 30 October 1987)

The influence of saturation and Stark shifting on the collisionless coherent anti-Stokes Raman scattering (CARS) spectra of Q-branch vibrational transitions has been studied theoretically and experimentally. These processes can significantly affect the magnitude and the spectral distribution of the CARS signal at the input power levels required to obtain detectable signals in typical low-pressure CARS experiments. The theory is developed with use of the Placzek approximation and rotation-vibration Bloch equations are obtained. The Doppler effect, nonresonant susceptibility, and spatial variation of power density in the probe volume are neglected. The Rabi frequency is found to increase with the square root of the final-state vibrational quantum number while the Stark frequency is nearly independent of this quantity. In order to understand the nature of some of the effects observed in scanning CARS, approximate analytic solutions are given for simple cases and CARS output spectra are obtained as a function of detuning. A Rabi-split response spectrum is found for all J with a Stark-induced asymmetry favoring the lower-frequency peak. Although the orientational degeneracy is lifted by both the Rabi and Stark terms, only a very weak dependence on the rotational quantum number is found in the spectral distribution; this allows use of the unsaturated rotational-quantum-number scaling in the saturated regime. It is apparent that the deviations due to saturation are weak for rotational temperature measurements while they are important for vibrational temperature measurements. Experimental results for low-pressure (2–5 mbar) nitrogen are also discussed. Appreciable deviations due to saturation and Stark effects are found for pump laser and Stokes power density products greater than 30 $(\mathrm{GW/cm^2})^2$. Semiquantitative agreement with theory is obtained for the observed dependences on power and on rotational and vibrational quantum numbers. A method allowing quick correction of saturated experimental data is proposed.

I. INTRODUCTION

Saturation of the Raman transitions is, together with dielectric breakdown, one of the main limiting mechanisms in the quantitative application of coherent anti-Stokes Raman scattering (CARS) as a diagnostic tool. The saturation phenomenon, which has received considerable attention recently,[1–15] involves significant redistribution of the populations of the states coupled by the Raman transition during the application of the driving pump fields (laser and Stokes fields). It is often observed as a consequence of the high pump intensities which are required to obtain measurable anti-Stokes signals from low-concentration molecular species. Concomitantly, because of low species concentration, there are typically no significant changes in the pump fields. In the absence of collisions, the regime which we will consider in this paper, there can also be sidebands (Rabi oscillations) which develop on the nonlinear signal due to the dynamical nature of the population redistribution. The problem becomes difficult to analyze when electronic resonance enhancement is present; this case has received attention recently,[5,6,13] but will not be covered here.

In addition to the dynamic population redistribution due to the saturation process, there is also a shifting[16–18] of the energies of the levels involved in the Raman process due to the separate presence of the laser and Stokes fields. For simplicity in further discussion we will describe the dynamical population redistribution as a Rabi process and the optical shift effects as a Stark process; both are a consequence of the electric dipole term in the coupling between the radiation field and the molecules.

This paper will develop the theory of CARS saturation by reducing the problem to an effective two-level model appropriate to conditions where single-photon resonances are absent. The following results are obtained for vibrational CARS.

(1) The Rabi frequency, and hence the degree of saturation and broadening, are proportional to the square root of the final-state vibrational quantum number. In contrast, the Stark shift of the transition frequency is found to be nearly independent of this quantity.

(2) The CARS spectrum splits into two components separated from the normal CARS polarization frequency by the Rabi frequency.

(3) The flux dependence of the peak CARS signal due to the Rabi process goes from $\Phi_1^2\Phi_2$ in the unsaturated case to Φ_1 in the fully saturated regime (1 denotes the pump laser field and 2 the Stokes field). The flux dependence of the linewidth increases as $(\Phi_1\Phi_2)^{1/2}$.

(4) The effect of the Stark shifts of the two Raman levels is to produce a negative shift in the Raman resonance frequency. The shift, which temporally varies in magnitude as the pump pulses vary, is an additional source of broadening and signal decrease.

(5) For Q-branch transitions, the optical shifts produce effects which are found to be comparable to the dynamical population redistribution terms; however, the magnitude of the saturation term can be reduced relative to the optical shift terms by making the ratio of the laser intensity to the Stokes intensity much larger or much smaller than unity.

(6) Orientational degeneracy is lifted by both the Stark and Rabi processes. This degeneracy lifting[19] is found to only have a very weak effect on rotational quantum number in the orientationally averaged CARS spectra. Thus the unsaturated rotational quantum number scaling of the spectral intensities is appropriate in the saturated regime.

We will also discuss observation of these processes in experiments carried out in a low-pressure (2–5 mbar) nitrogen discharge. At these low pressures and with 10 ns pump pulses, the radiation-molecule interaction can be considered to be occurring collisionlessly. The laser, Stokes, and anti-Stokes wavelengths are 532, 607, 473 nm, respectively, and are far from electronic resonances, which lie beyond 200 nm. A strong dependence of the saturation on vibrational quantum number has been observed. Semiquantitative agreement has been found between theory and experiment for the dependence on pump powers and on rotational and vibrational quantum number. The theory has been extended to the multifrequency pump case in order to account for the use of a multimode dye laser as the Stokes source. A more complete account of these experimental results has been published elsewhere.[20]

II. THEORY OF SATURATION IN CARS

A. General considerations

It is very convenient, in the theoretical analysis, to reduce the dynamical problem to one involving the two states of the Raman transition. This can be done to a high degree of approximation for molecules far from a single-photon resonance in two ways, both of which lead to the same result for the experimental conditions appropriate to this paper. The first approach is simply an extension of that used by Placzek[21] in his classical analysis of spontaneous Raman scattering. Placzek noted that for a molecule far from electronic resonance, the Born-Oppenheimer approximation can be used to express the interaction of the radiation with vibrational and rotational degrees of freedom in terms of the static electronic polarizability calculated as a function of time-independent nuclear coordinates. This analysis was extended by Garmire, Pandarese, and Townes[22] to unsaturated stimulated Raman scattering and to the saturated case by Giordmaine *et al.*[23] In the second approach, off-resonant density matrix terms are calculated by perturbation theory and substituted into the equations of motion for the resonant density matrix terms.[24–29] This "adiabatic elimination" has been used both for two-photon absorption (emission) and for the Raman case. The second technique is more general than the first but has the drawback that it cannot be readily related to the available literature on many electron calculations of molecular parameters. We will take the first approach since it is valid for the experiments described here where the optical frequencies are below the single-photon electronic resonances and the results can therefore be related to calculated polarizability parameters. We will incorporate the Stark terms in our analysis as a straightforward extension of the Placzek approach. The CARS term in the polarization response will involve a sum over the orientation states of the molecules in the fields. Since the strong fields will lift the orientational degeneracy, we must take these degeneracy lifting effects, which arise both from the Stark and Rabi processes, into account in our calculations.

The two-level Raman equations are very similar to the spin-$\frac{1}{2}$ equations in magnetic resonance and the two-level, single-photon equations often used in optics.[30,31] The interaction Hamiltonian for this reduced system is quadratic in the fields and has diagonal (level shifting) and off-diagonal (Raman coupling) terms in any unperturbed representation. The diagonal terms are the normal optical Stark terms while the off-diagonal terms lead to Rabi processes. Feynman, Vernon, and Hellwarth[32] have noted that any two-level system can be treated by a three-space Bloch vector model where the projections of any operator in the three directions are simply decompositions of the operator in terms of the three 2×2 spinors. The evolution of the density matrix can be shown to have the form of a torque equation in this three space with the result that the trace of the square of the density operator is an invariant. This vector model is a consequence of the fact that the two-level system forms the simplest representation of SU(2) and the invariant operator is simply related to the Casimir operator for this case. The invariance can be expressed as the well-known quadratic conservation law for the sum of the squares of half the population difference between the two levels and the square of the off-diagonal elements (polarizations). The vector model also allows one to conclude that there is an additional invariant for the special case when the torque vector is constant in direction. We shall see that this occurs in the rotating wave approximation for constant field amplitudes, or when the laser and Stokes amplitudes evolve identically in time on exact Raman resonance.

There have been a number of analytic solutions for the evolution of the collisionless Bloch equation in the rotating wave approximation for various constraints on the time-dependent external field. In the expository discussions given in this paper, we will make use of the time-independent exact solution, of the approximate solution[26,33] off resonance for smoothly varying (adiabatic) time dependences, and of the closed form solution on exact resonance.[31] On the other hand, for the detailed studies of the expected CARS signals from various Q-branch transitions in nitrogen, we will employ numerical techniques.

The CARS polarization $\mathbf{P}_3$ can be obtained from the general equation

$$\mathbf{P}_3 = N \,\mathrm{Tr}[\rho \vec{\alpha}(R)]\cdot\mathbf{E} \,, \tag{1}$$

where N is the number density of active molecules, index 3 denotes the anti-Stokes component, and the other symbols are defined as follows.

(a) The driving electric fields E are given by

$$\mathbf{E} = \hat{\epsilon}_\mu E_\mu \,, \tag{2}$$

where the summation is implicit, $\hat{\epsilon}_\mu$ is the polarization unit vector and E_μ is the scalar amplitude of the μth field. We write this amplitude as

$$E_\mu = \tfrac{1}{2}(E_\mu^{(+)} + E_\mu^{(-)}) = \tfrac{1}{2}(\mathcal{E}_\mu e^{i\mathbf{k}_\mu\cdot\mathbf{r} - i\omega_\mu t} + \text{c.c.}) \,, \tag{3}$$

where $(\pm)$ denote the positive and negative frequency components and $\mathcal{E}_\mu$ is the slowly varying part of the amplitude. We assume that the two input fields are linearly polarized in the same direction $\hat{\epsilon}$. We will also calculate the polarization component in the direction $\hat{\epsilon}$.

(b) The electronic polarizability tensor operator $\vec{\alpha}(R)$ is written in the Born-Oppenheimer approximation as a function of internuclear separation R. With our selection of field polarizations, we shall be making use, in Eq. (1), of the component

$$\alpha(R) = \hat{\epsilon}\cdot\vec{\alpha}(R)\cdot\hat{\epsilon} \,. \tag{4}$$

Note that $\alpha(R)$ depends implicitly on the orientation of the molecule in the field; $\alpha_\parallel(R)$ and $\alpha_\perp(R)$ are the tensor components along the molecular axis and orthogonal to it, respectively.

(c) The density operator ρ is obtained from its evolution equation as described in the following section.

B. Density operator

The density operator evolution equation is given in the collisionless regime by

$$i\hbar\frac{\partial\rho}{\partial t} = [\mathcal{H}^0 + \mathcal{H}^r, \rho] \,, \tag{5}$$

where 0 and r are used to denote the nonradiative and radiative parts of the Hamiltonian, respectively. In the Placzek approximation, the radiative part of the Hamiltonian takes on the form

$$\mathcal{H}^r = -\tfrac{1}{4}\alpha(R)E^{(+)}E^{(-)} \,. \tag{6}$$

We note that the force driving the vibration is given by the derivative of the polarization Hamiltonian with respect to the internuclear coordinate. There are two basic effects of radiation on the molecular system: the Stark shift and the Raman driving and saturation effect.

The Stark shift involves the terms in the Hamiltonian which are diagonal in the vibration-rotation states v,J,M. For the case of nitrogen, the ground electronic state is $^1\Sigma$, so that there are no electronic contributions to the total angular momentum. Only the very slowly varying parts of the intensity contribute significantly to the diagonal terms so that the diagonal part of the Hamiltonian may be approximated by

$$\mathcal{H}^r_{vJM,vJM} = -\tfrac{1}{4}(|\mathcal{E}_1|^2 + |\mathcal{E}_2|^2) \times(\Delta\alpha_{v,v}\langle JM|\cos^2\theta|JM\rangle + \alpha_{\perp v,v}) \,, \tag{7}$$

where $\Delta\alpha_{vv'} = \langle v|\alpha_\parallel - \alpha_\perp|v'\rangle$ and v,J,M are the vibrational, total rotational angular momentum, and orientational (magnetic) angular momentum quantum numbers, respectively. The angle θ is taken between $\hat{\epsilon}$ and the molecular internuclear axis. Note that for Q-branch transitions, the transition Stark shift is due only to the variation of the polarizability matrix element with vibrational quantum number. Using known expressions for spherical harmonics,[34] we have

$$C(J,M) = \langle JM|\cos^2\theta|JM\rangle = \frac{2(J^2-M^2)+2J-1}{(2J+3)(2J-1)} \,. \tag{8}$$

Equations (7) and (8) agree with the result obtained by Farrow and Rahn,[17] except that we have retained the rotationally-independent term. The contribution from the rotationally-independent term will be comparable to that from the rotationally-dependent term for Q-branch transitions, but much smaller than it for O- and S-branch transitions.

The off-diagonal radiation field terms (Raman driving and saturation effect) drive the vibration and produce the CARS signal. For the case of near-Raman resonance, the part of the off-diagonal portion of the interaction Hamiltonian which can resonate with the transition is given by

$$\mathcal{H}^r_{v'J'M',vJM} = -\tfrac{1}{4}\mathcal{E}_{1_1}\mathcal{E}_2^* e^{i(\mathbf{k}_1-\mathbf{k}_2)\cdot\mathbf{r}} e^{-i(\omega_1-\omega_2)t} \times(\Delta\alpha_{v',v}\langle J'M'|\cos^2\theta|JM\rangle + \alpha_{\perp v',v}\delta_{J',J})\delta_{M',M} \,. \tag{9}$$

We will neglect the rapidly varying antiresonant parts of the off-diagonal elements, i.e., we make the rotating wave approximation. Using (5), (7), and (9), we have for the relevant density matrix elements

$$i\frac{dp}{dt} = -\Delta\tilde{\omega}\,p + \Omega_R n \tag{10}$$

and

$$i\frac{dn}{dt} = 2(\Omega_R^* p - \text{c.c.}) \,, \tag{11}$$

where

$$p = \rho_{v'J'M,vJM} e^{+i(\omega_1-\omega_2)t} \,, \tag{12}$$

$$n = \rho_{vJM,vJM} - \rho_{v'J'M,v'J'M} \,, \tag{13}$$

$$\Delta\tilde{\omega} = \Delta\omega + \Omega_s \,, \tag{14}$$

$$\Delta\omega = \omega_1 - \omega_2 - \omega_0 \,, \tag{15}$$

$$\hbar\omega_0 = \mathcal{H}^0_{v'J'M} - \mathcal{H}^0_{vJM} \,, \tag{16}$$

$$\hbar\Omega_S = \mathcal{H}^r_{vJM,vJM} - \mathcal{H}^r_{v'J'M,v'J'M} \,, \tag{17}$$

and

$$\hbar\Omega_R = \mathcal{H}^r_{v'J'M,vJM} e^{i(\omega_1-\omega_2)t} \,. \tag{18}$$

Note that $M'=M$ from symmetry requirements. For simplicity in further discussion, we have suppressed the quantum states in writing Eqs. (10)–(18). For the most part in low-pressure CARS experiments, we deal with resonances involving transitions between states of specific vibrational and total angular momentum quantum numbers. In unsaturated CARS the states of specific magnetic quantum number which are energy degenerate contribute in varying degrees to the strength of the CARS signal; however, their spectral positions and shapes are identical. In saturated CARS, the orientational degeneracy is lifted by the optical fields and the spectral profiles can be affected by the magnetic quantum number M.

In the case of a diatomic such as nitrogen, we only have a single internuclear coordinate, and the polarizability depends on its magnitude. If we expand about the equilibrium internuclear position for small vibrational displacements, we find to second order

$$\alpha_{\parallel}(R)=\alpha_{\parallel 0}+\left.\frac{d\alpha_{\parallel}}{dR}\right|_{R=R_0} q+\frac{1}{2}\left.\frac{d^2\alpha_{\parallel}}{dR^2}\right|_{R=R_0} q^2+\cdots , \tag{19}$$

where $\alpha_{\parallel 0}=\alpha_{\parallel}(R=R_0)$ and similarly for $\alpha_{\perp}$. Here q is the displacement from the equilibrium value:

$$q=R-R_0 . \tag{20}$$

Expressing (17) in terms of (19) and keeping only low-order nonvanishing terms we find

$$\Omega_S=-\frac{\Delta\alpha_0}{4\hbar}(|\mathcal{E}_1|^2+|\mathcal{E}_2|^2) \times(\langle JM|\cos^2\theta|JM\rangle-\langle J'M|\cos^2\theta|J'M\rangle) , \tag{21a}$$

with $\Delta\alpha_0=\alpha_{\parallel 0}-\alpha_{\perp 0}$, for O- and S-branch transitions, where $J'=J\pm 2$ and

$$\Omega_s=-\frac{1}{4\hbar}(|\mathcal{E}_1|^2+|\mathcal{E}_2|^2) \times\left[\left[\left.\frac{d\Delta\alpha}{dR}\right|_{R=R_0}(\langle v|q|v\rangle-\langle v'|q|v'\rangle)+\frac{1}{2}\left.\frac{d^2\Delta\alpha}{dR^2}\right|_{R=R_0}(\langle v|q^2|v\rangle-\langle v'|q^2|v'\rangle)\right]\langle JM|\cos^2\theta|JM\rangle + \left.\frac{d\alpha_{\perp}}{dR}\right|_{R=R_0}(\langle v|q|v\rangle-\langle v'|q|v'\rangle)+\frac{1}{2}\left.\frac{d^2\alpha_{\perp}}{dR^2}\right|_{R=R_0}(\langle v|q^2|v\rangle-\langle v'|q^2|v'\rangle)\right] , \tag{21b}$$

for Q-branch transitions.

Nonzero diagonal elements of the vibrational coordinate q arise from odd-order anharmonic terms in the vibrational energy. It is expected that the second polarizability term in (21b), which is a second-order correction, is of the same order as the first term which is the product of the first-order term in the polarizability and a term which involves a first-order correction to the vibrational wave function arising from the anharmonic potential.

Similarly for the Rabi-Raman term (16), we find

$$\Omega_R=-\frac{1}{4\hbar}\mathcal{E}_1\mathcal{E}_2^* e^{i(\mathbf{k}_1-\mathbf{k}_2)\cdot\mathbf{r}} \times\left[\left.\frac{d\Delta\alpha}{dR}\right|_{R=R_0}\langle J'M|\cos^2\theta|JM\rangle + \left.\frac{d\alpha_{\perp}}{dR}\right|_{R=R_0}\right]\langle v'|q|v\rangle . \tag{22}$$

We will now consider the magnitude of the various Stark shift terms given in (21a) and (21b). In order to obtain nonvanishing diagonal elements of the term linear in vibrational coordinate in (21b), we must take into account the anharmonicity of the vibration. We assume a Morse potential of the form

$$V(q)=D_e(1-e^{-\beta q})^2 , \tag{23}$$

where D_e is the dissociation energy and

$$\beta=\left[\frac{\mu}{D_e}\right]^{1/2}\omega_e , \tag{24}$$

where μ is the reduced mass and ω_e is the harmonic contribution to the vibrational frequency. Retaining only the cubic contribution to the anharmonicity, we find from perturbation theory

$$\langle v|q|v\rangle=\frac{3\hbar}{2}\left[\frac{1}{\mu D_e}\right]^{1/2}(v+\tfrac{1}{2}) =1.2\times 10^{-10}(v+\tfrac{1}{2})\text{ cm} , \tag{25}$$

where the numerical value has been obtained using the spectroscopic constants for nitrogen.[35] Equation (25) together with the first derivative term in Eq. (21b) are equivalent to the classical mechanical result of Rahn *et al.*[16] The quadratic term is nonvanishing in the harmonic approximation and is given by

$$\langle v|q^2|v\rangle=\frac{\hbar}{\mu\omega_e}(v+\tfrac{1}{2}) =0.21\times 10^{-18}(v+\tfrac{1}{2})\text{ cm}^2 . \tag{26}$$

Again the numerical value is obtained using the spectro-

scopic constants for nitrogen.

The components of the polarizability tensor have been calculated for N_2 as a function of internuclear separation by Morrison and Hay.[36] These authors give results for both Hartree-Fock and generalized valence-bond (perfect pairing) calculations; we consider only the latter as it presumably represents a more accurate method. The polarizability and its first and second derivatives are given in Table I. It is apparent from the table and Eqs. (25) and (26) that for N_2 the first-order term is about ten times as large as the second-order term in (21b). In addition, it is clear from the table and Eqs. (21a), (21b), (25), and (26) that the O- and S-branch terms can be almost one order of magnitude larger than the Q-branch term for the lower-J values. Note that the contribution of the second polarizability derivative is small and is found only in the calculation of Ω_S. Since its calculation is imprecise, it is neglected in the numerical calculations which follow.

To estimate the magnitude of the Rabi-Raman term (22), we note that in the harmonic approximation,

$$\langle v \mid q \mid v' \rangle = \left[\frac{\hbar}{2\mu\omega_e}\right]^{1/2} [(v+1)^{1/2}\delta_{v+1,v'} + v^{1/2}\delta_{v-1,v'}]$$
$$= 0.32\times 10^{-9}[(v+1)^{1/2}\delta_{v+1,v'} + v^{1/2}\delta_{v-1,v'}] \text{ cm} . \quad (27)$$

If the driving fields 1 and 2 are comparable in magnitude, then, for low v, the Rabi-Raman term is roughly an order of magnitude smaller than the O- and S-branch Stark shifts while it is about an order of magnitude larger than the Q-branch Stark shift. Also note that the Stark shift Ω_S is independent of vibrational quantum number while the Rabi-Raman term Ω_R grows as the square root of the quantum number of the upper state.

C. Anti-Stokes polarization

In Eq. (10), p is the Raman-induced coherence which will drive the anti-Stokes polarization and n is the population difference probability between the lower and higher vibration rotation states. Note that p is complex with the real and imaginary components being out of phase and in phase, respectively, with the phase defined by the difference between the phases of the input driving fields.

TABLE I. Polarizability and polarizability derivatives, after Morrison and Hay (Ref. 36). The calculation of the second-order derivative is very imprecise.

	α (10^{24} cm^3)	$\left.\frac{d\alpha}{dR}\right\|_{R=R_0}$ (10^{16} cm^2)	$\left.\frac{d^2\alpha}{dR^2}\right\|_{R=R_0}$ (10^8 cm)
Parallel	2.0	2.4	−1.5
Perpendicular	1.4	1.1	−0.1
Difference	0.6	1.3	−1.4

The anti-Stokes radiation field is driven by the macroscopic polarization $\mathbf{P}_3$. Using the general equation for the polarization, Eq. (1), we can write the component of $\mathbf{P}_3$ in the direction of the input fields

$$P_3(r,t) = \tfrac{1}{2}N \sum_{v,v',J,J',M} \rho_{v'J'M,vJM} \times (\Delta\alpha_{vv'}\langle JM \mid \cos^2\theta \mid J'M\rangle + \alpha_{\perp vv'}\delta_{JJ'})\mathcal{E}_1 e^{i(\mathbf{k}_1\cdot\mathbf{r}-\omega_1 t)} + \text{c.c.} \quad (28)$$

Here only the laser field appears since it is the only frequency component which beats with the Raman-induced polarizability to produce the anti-Stokes polarization. Note that the rotational dependence appears both in the density matrix elements and in the polarizability operator element; it is the product of these elements which is angularly averaged by the sum over rotational states. We see from Eqs. (14) and (15) that only the density matrix elements which are off diagonal in the vibrational quantum numbers can oscillate at $\omega_1-\omega_2$. The polarization can be expressed as

$$P_3(t) = \tfrac{1}{2}N\mathcal{E}_1 e^{-i[(2\omega_1-\omega_2)t-2\mathbf{k}_1-\mathbf{k}_2\cdot\mathbf{r}]} \times \sum_{v,v',J,J',M} p\langle v \mid q \mid v'\rangle \left[\left.\frac{d\Delta\alpha}{dR}\right|_{R=R_0}\langle JM \mid \cos^2\theta \mid J'M\rangle + \left.\frac{d\alpha_\perp}{dR}\right|_{R=R_0}\delta_{JJ'}\right] + \text{c.c.} \quad (29)$$

Note that p depends on v, v', J, J', and M.

Integrating spatially to get the output anti-Stokes field, squaring to get the intensity I_3, and time integrating to get the flux, we find

$$\Phi_3 = \int_{-\infty}^{\infty} dt\, I_3 = K\frac{N^2}{4}\int_{-\infty}^{\infty} dt \mid \mathcal{E}_1 \mid^2 \left| \sum_{v,v',J,J',M} p\langle v \mid q \mid v'\rangle \left[\left.\frac{d\Delta\alpha}{dR}\right|_{R=R_0}\langle JM \mid \cos^2\theta \mid J'M\rangle + \left.\frac{d\alpha_\perp}{dR}\right|_{R=R_0}\delta_{JJ'}\right]\right|^2 , \quad (30)$$

where the 3 subscript denotes the anti-Stokes field and where K is a constant which depends on cell length and phase-matching conditions. The off-diagonal component of the density matrix is complex, thus there can be variations in phase between the terms in the summation and hence partial cancellation between terms. From Eqs. (29) and (30) one can obtain the important quantities which are measured experimentally: CARS line shapes when ω_2

is tuned over the resonances, and spectral broadening of the anti-Stokes field resulting from Rabi oscillations (apparently not yet observed in CARS experiments). Some of these effects can be described theoretically using analytic solutions; others require numerical computations. These subjects are covered in the following sections.

D. CARS line shapes and power dependence

We now consider solutions to the Raman-Stark dynamical Eqs. (10) and (11). These equations are similar to the Bloch equations for a dipole-transition-coupled two-level system except that the product of the dipole by a single field amplitude is replaced by a factor which involves the product of polarizability derivatives, the amplitude of input field 1 and the amplitude of input field 2. The present result also includes the Stark effect due to the two input-exciting fields, a term generally neglected in the simple two-level approximation.

Equations (12) and (13) are linear coupled equations with time-dependent coefficients. The Rabi term Ω_R varies in time as the product of the slowly varying field amplitudes $\mathcal{E}_1\mathcal{E}_2^*$. By slowly varying, we mean to imply that the variation is slow not only with respect to the optical periods but also with respect to the period of the vibration-rotation transition. No assumption need be made about the pulse variation in comparison to the time $1/\Delta\omega$. $\Delta\tilde{\omega}$ also varies in time because of the optical Stark effect term Ω_S which follows the time dependence of the sum of the input intensities.

These equations obey the well-known 2×2 spinor or Bloch-vector conservation law[32]

$$\frac{d\,|p|^2}{dt}+\frac{1}{4}\frac{dn^2}{dt}=0\ , \tag{31}$$

which is equivalent to the Casimir invariant for the two-level representation of SU(2). The CARS signal is proportional to

$$|p|^2=\tfrac{1}{4}[n_0^2-n^2(t)]\ , \tag{32}$$

where n_0 is the initial population difference probability between the lower and upper vibration-rotation states.

Equation (32) shows that population change takes place whenever a CARS signal is generated. Also, $|p|$ can never exceed $\frac{1}{2}n_0$. In addition to saturation, there is also power broadening of the CARS line. This broadening will be negligible compared to the pulse width transform broadening provided $\Omega_R t_p \ll 1$, where t_p is the pulse duration. We now proceed with a detailed presentation of the theoretical results.

1. Square pulse case

The exact solutions for constant driving field amplitudes have been given previously. For this square pulse case, we will describe the solution for $|p|^2$ which, in the nondegenerate case (i.e., $J=0$, $M=0$ Q-branch transition), is proportional to the anti-Stokes signal. We will find that certain spectral characteristics of the square pulse are preserved for cases of more realistic pulse shapes. The expression for $|p|^2$ is

$$|p|^2=\frac{2n_0^2\Omega_R^2}{[(\Delta\tilde{\omega})^2+(2\Omega_R)^2]^2}\times\{(\Delta\tilde{\omega})^2+\Omega_R^2-(\Delta\tilde{\omega})^2\cos\varphi(t)-\Omega_R^2\cos[2\varphi(t)]\}\ , \tag{33}$$

where

$$\varphi(t)=[(\Delta\tilde{\omega})^2+(2\Omega_R)^2]^{1/2}t\ .$$

If $\Omega_R t_p \gg 1$, where t_p is the pulse length, we can drop the oscillating terms[8] and we find for the average value of $|p|^2$:

$$\overline{|p|^2}=2n_0^2\frac{\Omega_R^2[(\Delta\tilde{\omega})^2+\Omega_R^2]}{[(\Delta\tilde{\omega})^2+(2\Omega_R)^2]^2}\ . \tag{34}$$

This solution is different, when $\Delta\tilde{\omega}\gg\Omega_R$, from the adiabatic following solution which is appropriate for a smoothly varying pulse. As shown in Fig. 1, $\overline{|p|^2}$ has two maxima offset from $\Delta\tilde{\omega}=0$ by $\Delta\tilde{\omega}=\pm\sqrt{2}\Omega_R$, with peak values of $\frac{1}{6}n_0^2$. The central minimum at $\Delta\tilde{\omega}=0$ has a value of $\frac{1}{8}n_0^2$, thus the ratio of the side maxima to the central minimum is $\frac{4}{3}$. In addition to the Rabi splitting of $2\sqrt{2}\Omega_R$, there is a broadening with a full width at half maximum of $2\sqrt{2}(4+\sqrt{17})^{1/2}\Omega_R$, which is of the order of three times the Rabi splitting. The far wings are Lorentzian ($\Delta\tilde{\omega}\gg\Omega_R$). Note that Agarwal and Sing[10] and Lucht and Farrow[14] have calculated similar line

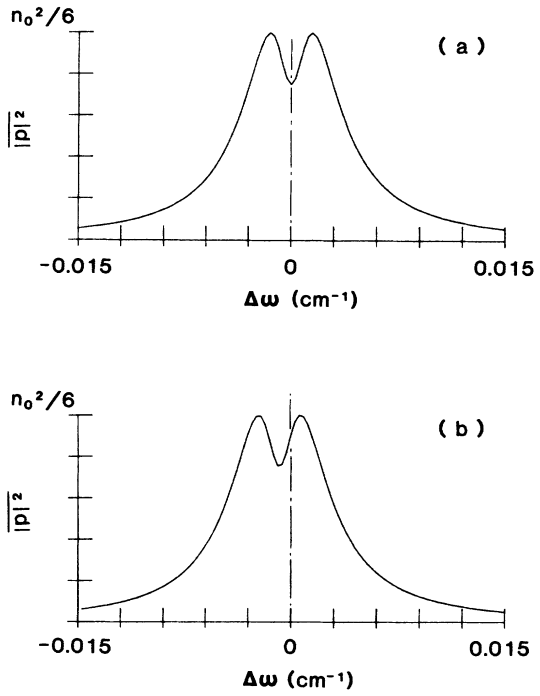

FIG. 1. Plot of $\overline{|p|^2}$ vs $\Delta\omega$ (similar to CARS spectrum) for square wave amplitude laser and Stokes pulses. (a) The Stark effect is neglected and (b) the Stark effect is included. The molecular parameters are for the (1,0,0)←(0,0,0) transition in N_2 where the notation (v,J,M) is used. Also, $I_1=4\times10^9$ W/cm^2 and $I_2=1.33\times10^9$ W/cm^2.

shapes; theirs, however, are asymmetric due to nonresonant background interference. When Ω_R increases, $|p|^2$, as given by (34), expands along the frequency axis about $\Delta\omega=0$, but its shape and amplitude are conserved if the Stark effect is negligible.

In the limit where saturation is negligible, so that $n\approx n_0$, we can readily solve (10) for p to find, for any pulse shape and arbitrary $\Delta\tilde{\omega}$

$$|p|^2=n_0^2\left|\int_{-\infty}^{t}dt'\Omega_R(t')\exp\left[i\int_{-\infty}^{t'}\Delta\tilde{\omega}(t'')dt''\right]\right|^2 . \tag{35}$$

If the Stark-shift frequency chirp is negligible so that $\Delta\tilde{\omega}=\Delta\omega$, we then have

$$|p|^2=n_0^2\left|\int_{-\infty}^{t}dt'\,e^{i\Delta\omega t'}\Omega_R(t')\right|^2 , \tag{36}$$

a form which is readily integrated for simple driving pulse shapes. For a square wave pulse we can find the unsaturated limit either from (36) or by expanding (33). From (33), we obtain

$$|p|^2=4n_0^2\left(\frac{\Omega_R}{\Delta\tilde{\omega}}\right)^2\sin^2\left(\frac{\Delta\tilde{\omega}\,t}{2}\right)\quad\text{for } 0\le t\le t_p$$

and (37)

$$|p|^2=4n_0^2\left(\frac{\Omega_R}{\Delta\tilde{\omega}}\right)^2\sin^2\left(\frac{\Delta\tilde{\omega}\,t_p}{2}\right)\quad\text{for } t\ge t_p .$$

In the case $\Delta\tilde{\omega}t_p\ll 1$, Eqs. (37) simplify to

$$|p|^2=n_0^2\Omega_R^2t^2\quad\text{for } 0\le t\le t_p$$

and (38)

$$|p|^2=n_0^2\Omega_R^2t_p^2\quad\text{for } t\ge t_p .$$

Using these square pulse results we can come to some simple conclusions concerning the dependence of the anti-Stokes output flux on the laser and Stokes input fluxes. Two limiting cases are the following.

(1) Unsaturated case, on resonance. Using the fact that for a square pulse $\Omega_R^2t_p^2\propto\Phi_1\Phi_2$, we find from (30) and (38)

$$\Phi_3=K_1\Phi_1^2\Phi_2 , \tag{39}$$

where K_1 is a constant. This is the normal unsaturated result. This is also the ideal situation for CARS measurements. Equation (39) remains valid so long as population saturation or spectral broadening are avoided. To this end, one has to limit the product Ω_Rt_p, which is equivalent to limiting $\Phi_1\Phi_2$. The signal flux is thus optimized by using a large Φ_1 and a small Φ_2. One also notes that this flux does not depend explicitly on t_p, the pulse duration.

(2) Saturated case, on resonance. Using (30) and (34) with the provision $\Omega_R\gg|\Delta\tilde{\omega}|$, we find that

$$\Phi_3=K_2\Phi_1 . \tag{40}$$

Again, K_2 is a constant. This equation shows that the signal is proportional to the pump flux at ω_1. It is also independent of t_p, as in the unsaturated case. Equation (40) is a consequence of the fact that p executes many oscillations at frequency Ω_R during the pulse and that its average value is independent of these oscillations (i.e., of Ω_R or, equivalently, $\sqrt{I_1I_2}$). It is apparent from (40) that, in the fully saturated limit, shortening the pump pulse at ω_1 while holding the pulse energy constant does not enhance the anti-Stokes signal.

Collisions strongly influence the CARS signal. In particular, differences in rotational and vibrational relaxation times play an important role in the dynamical behavior.[7] For atmospheric pressure N_2 and nanosecond pulses, Lucht and Farrow[14] have shown the signal to be generated only at the beginning of the pulse. This is a consequence of redistribution of molecular population within the rotational manifolds of the upper and lower vibrational states coupled by the Raman transition. We thus have $n\to 0$ and $p\to 0$ for $t>\tau_r$, where τ_r is the rotational redistribution time. The CARS signal will be optimized if redistribution is negligible during the pulse (i.e., if $t<\tau_r$).

It can also be shown that far-off resonance, such that $\Delta\omega\gg\Omega_R, t_p^{-1}$ the anti-Stokes flux has the form

$$\Phi_3=K_3\Phi_1^2\Phi_2\frac{1}{(\Delta\omega\,t_p)^2} , \tag{41}$$

which is the same flux dependence as the unsaturated case on resonance.

We have thus seen that the Rabi saturation manifests itself in the anti-Stokes spectrum as (1) Rabi splitting, (2) Rabi broadening, (3) a change, near line center, in the dependence of anti-Stokes flux on laser and Stokes fluxes.

2. *Arbitrary pulse shapes*

In order to make the theoretical results more directly comparable to experiment, we have numerically calculated the anti-Stokes flux for a Gaussian pulse. If the Stark effect is neglected, we obtain the CARS spectrum as shown in Fig. 2. The structure is similar in appearance to the square-pulse case; the two distinct Rabi peaks are maintained despite the fact that the Rabi frequency varies throughout the pulse.

When the Stark-shift term is included, so that the transition frequency chirps during the pulse with a magnitude similar to the Rabi frequency, we obtain the results shown in Fig. 3. Apparent are an overall negative frequency shift of the spectrum and an asymmetry in the height of the Rabi peaks. The asymmetry in favor of the lower frequency peak can be qualitatively understood by noting that, for the lower frequency peak, the Stark shift acts to maintain the lower Rabi shift resonance as the lower Rabi frequency first increases then decreases during the pulse. Lucht and Farrow have reported similar experimental and theoretical line shapes.[14]

As we have noted earlier, the Rabi and Stark effects lift the orientational degeneracy. In order to understand this case, it is useful to express for a Q-branch transition the Rabi frequency, using (8), (22), and (27), as

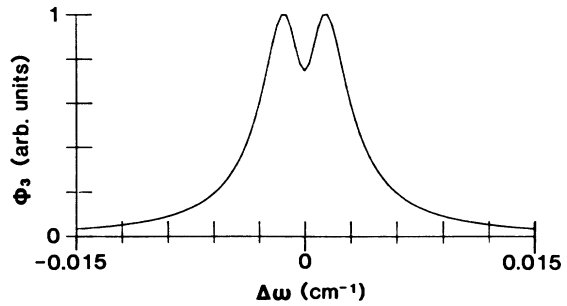

FIG. 2. Calculated CARS spectra for peak power densities $I_1=6\times10^9$ W/cm^2 and $I_2=2\times10^9$ W/cm^2. Pulses are Gaussians with a full width at $1/e$ of 10 ns; Stark effect is neglected. Collected flux is given in arbitrary units.

$$\Omega_R=-\frac{1}{4}\left[\frac{1}{2\mu\hbar\omega_e}\right]^{1/2}\left.\frac{d\alpha_\perp}{dR}\right|_{R=R_0}\mathcal{E}_1\mathcal{E}_2^*(v+1)^{1/2}\times A_R(J,M)\ , \tag{42}$$

where

$$A_R(J,M)=\Gamma_R C(J,M)+1\ , \tag{43}$$

and

$$\Gamma_R=\left.\frac{d\Delta\alpha}{dR}\right|_{R=R_0}\left[\left.\frac{d\alpha_\perp}{dR}\right|_{R=R_0}\right]^{-1}\ , \tag{44}$$

and $C(J,M)$ is given by (8). For N_2, $\Gamma_R=(2.25-0.86)/0.86=1.62$.

Similarly, we can obtain, in the Morse potential approximation, using (8), (21b), (25), and (26), an expression for the Stark frequency

$$\Omega_S=-\frac{1}{8}\left[3\left[\frac{1}{\mu D_e}\right]^{1/2}\left.\frac{d\alpha_\perp}{dR}\right|_{R=R_0}+\frac{1}{\mu\omega_e}\left.\frac{d^2\alpha_\perp}{dR^2}\right|_{R=R_0}\right]\times(|\mathcal{E}_1|^2+|\mathcal{E}_2|^2)A_S(J,M)\ , \tag{45}$$

where

$$A_s(J,M)=\Gamma_s C(J,M)+1 \tag{46}$$

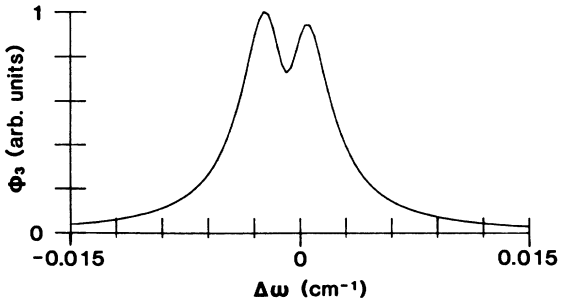

FIG. 3. Same as Fig. 2 except that Stark effect is included; same vertical scale as in Fig. 2.

and

$$\Gamma_S=\frac{\left[3\left[\frac{1}{\mu D_e}\right]^{1/2}\left.\frac{d\Delta\alpha}{dR}\right|_{R=R_0}+\frac{1}{\mu\omega_e}\left.\frac{d^2\Delta\alpha}{dR^2}\right|_{R=R_0}\right]}{\left[3\left[\frac{1}{\mu D_e}\right]^{1/2}\left.\frac{d\alpha_\perp}{dR}\right|_{R=R_0}+\frac{1}{\mu\omega_e}\left.\frac{d^2\alpha_\perp}{dR^2}\right|_{R=R_0}\right]}\ . \tag{47}$$

For nitrogen, in view of the discussion of Eqs. (21) and (22), we can neglect the second derivative terms, so that $\Gamma_S\simeq\Gamma_R=\Gamma$ and $A_s(J,M)\approx A_R(J,M)\equiv A(J,M)$.

$A(J,M)$ has limiting values at $M=0$ and $M=J$. These are

$$A(J,0)=\left[\frac{2J^2+2J-1}{(2J+3)(2J-1)}\Gamma+1\right] \tag{48}$$

and

$$A(J,J)=\left[\frac{1}{(2J+3)}\Gamma+1\right]\ .$$

The results for the limiting M values are plotted versus J in Fig. 4. It is noteworthy that the ratio of maximum and minimum values of $A(J,M)$ is less than a factor of 2 and that these values straddle the $J=0$, $M=0$ value. Thus the degeneracy is in effect only weakly lifted, and the addition of the orientational contributions for an arbitrary J state will produce a CARS spectrum having nearly the same form as that for the $J=0$, $M=0$ case but with a weight which is given by the square of the degeneracy factor, $2J+1$.

Figure 5 shows the calculation of the CARS line shape divided by $(2J+1)^2$ for the transitions $(1,12,M)\leftarrow(0,12,M)$, together with the curve from Fig. 3 [i.e., that corresponding to the transition $(1,0,0)\leftarrow(0,0,0)$]. The slight difference between the two curves illustrates a weak increase of saturation as a function of J. The ratio of cor-

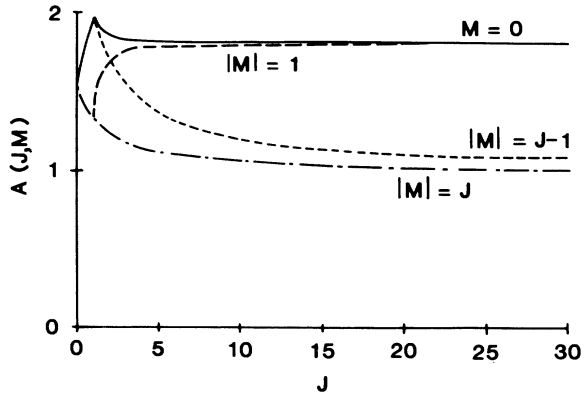

FIG. 4. Plot of limiting values for $|M|=0,1$ and $|M|=J,J-1$ of $A(J,M)$ vs J. $A(J,M)$ is the rotational-state-dependent factor in the Rabi and Stark frequencies. For $J=0$, we have $A(0,0)=(\frac{1}{3}\Gamma+1)$ or 1.54 for N_2. When $J\to\infty$, we have $A(J\to\infty,0)=(\frac{1}{2}\Gamma+1)$ or 1.81 for N_2 and $A(J\to\infty,J\to\infty)=1$.

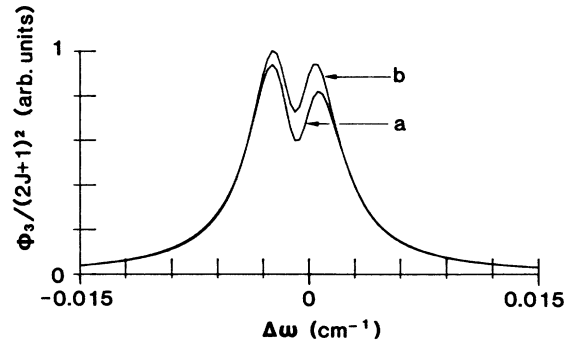

FIG. 5. Same as Fig. 3 except that the transitions $(1,12,M)\leftarrow(0,12,M)$ are used (a). The curve of Fig. 3 is shown for comparison (b).

responding CARS line amplitudes is here about 600. In the absence of saturation, this ratio would be exactly 625.

E. Fourier analysis of anti-Stokes wave

We have so far considered the dependence of the CARS output energy on the input frequency. In other words, we have treated the tuning of the Stokes (or laser) radiation as the spectral probe. It is also instructive to consider the spectral character of the anti-Stokes radiation at particular fixed values of the laser and Stokes frequencies or, more pertinently, at a fixed detuning from the Raman resonance. This output spectrum could be measured with a spectrometer or by a heterodyne technique. That there will be more than one spectral component is apparent from Eqs. (10) and (11) which, for constant amplitude pumping fields, have two homogeneous and one inhomogeneous solutions. We shall see that the homogeneous solutions do not appear when we make the adiabatic following approximation for $\Delta\omega \gg \Omega_R$. Agarwal and Singh[10] also have noted that the CARS signal spectrum should possess sidebands when cw pump lasers with stochastic pump fluctuations are used.

The anti-Stokes spectral density is related to the spectral density of the off-diagonal density matrix element as follows:

$$|E_3(\omega)|^2 \propto |p(\nu)|^2 , \tag{49}$$

where $\nu=\omega-(2\omega_1-\omega_2)$. For a square driving pulse we find

$$|p(\nu)|^2 \propto n_0^2 \frac{\Omega_R^2}{\Omega^4}[4\Delta\tilde{\omega}^2 S(\nu)+(\Delta\tilde{\omega}+\Omega)^2 S(\nu+\Omega) + (\Delta\tilde{\omega}-\Omega)^2 S(\nu-\Omega)] , \tag{50}$$

where

$$\Omega^2=(\Delta\tilde{\omega})^2+(2\Omega_R)^2$$

and

$$S(\nu)=\frac{\sin^2(\nu t_p)}{\nu^2} .$$

Note that this equation holds even in the presence of Stark shifting. $S(\nu)$ is a sharply peaked function and, if $\Omega t_p \gg 1$, we may take it to have the form $\pi t_p \delta(\nu)$. A three-dimensional plot showing the location and amplitude of the three peaks is presented in Fig. 6 as a function of detuning from the molecular resonance. The curve projecting onto the $\Delta\tilde{\omega}$ axis corresponds to the first term in (50); this term peaks at $\Delta\tilde{\omega}=\pm 2\Omega_R$ and is zero at $\Delta\tilde{\omega}=0$. The second and third terms correspond to the curves projecting onto the upper and lower hyperbolae, respectively. They have peaks at $\pm 2\Omega_R/\sqrt{3}$ for the lower and upper curves, respectively. They have a very small value when the curves approach their asymptotes (dashed lines), and these values then are close to the value of the first term.

Note that when we sum the intensities of the three spectral components we obtain an expression having the same form as Eq. (34). Thus for the square-pulse case the intensity of the CARS signal at a given detuning is simply a sum of the intensities of the district spectral features which appear at the particular detuning.

We now turn to the question of the spectral character of the anti-Stokes spectra expected for temporally smooth laser and Stokes pulses at a fixed detuning from resonance. For a sufficiently smooth pulse applied off resonance, we expect to find spectra consistent with the approximate analytic solutions given for adiabatic following. In addition, on resonance we find a novel analytic solution for the response which gives a spectrum with interference peaks which follow an Airy-like pattern.

In order to readily obtain these approximate analytic solutions it is useful to transform the Bloch equations (10) and (11) into the well-known pseudovector form:

$$\frac{dp''}{dt}=\Delta\omega p'-2\Omega_R(t)n , \tag{51}$$

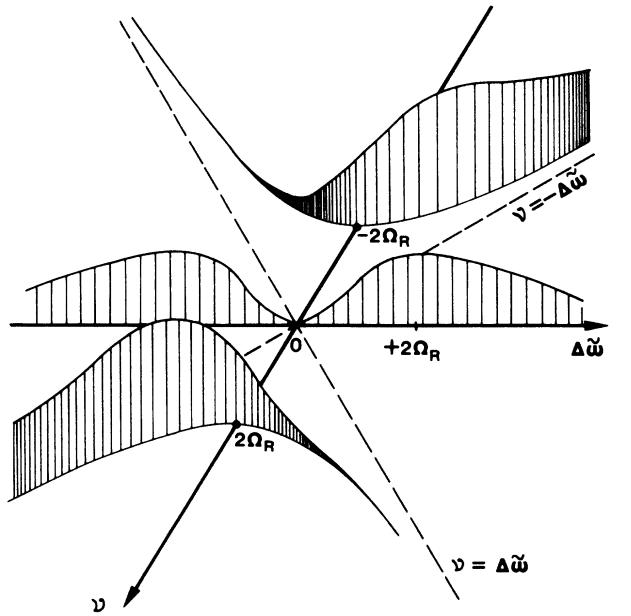

FIG. 6. Frequencies and amplitudes of the three peaks in the anti-Stokes spectrum about the center frequency $\nu=0$ as a function of $\Delta\tilde{\omega}$ for square input field pulse shapes.

$$\frac{dp'}{dt} = -\Delta\omega p'' , \tag{52}$$

$$\frac{dn}{dt} = 2\Omega_R(t)p'' , \tag{53}$$

where

$$p' = 2\,\mathrm{Re}(p), \quad p'' = 2\,\mathrm{Im}(p)$$

and the Stark effect is now neglected.

In the vector model p', p'', and n can be treated as the components of a three-dimensional polarization-population difference vector and $2\Omega_R$, 0, and $\Delta\omega$ treated as the components of a second vector, the Rabi frequency-detuning frequency vector. The rate of change of the polarization-population difference vector is equal to the cross product between the polarization-population difference vector and the Rabi frequency-detuning frequency vector. The conservation law (Casimir invariant) given by Eq. (31) is an obvious consequence of this vector form.

The adiabatic solution is found by assuming that the input pulse varies sufficiently slowly so that we can neglect the left-hand side of (51), to obtain

$$\Delta\omega p' = 2\Omega_R(t)n . \tag{54}$$

If we further assume $n, p' \gg p''$ then from the conservation law (31) we find

$$n = \frac{n_0}{\left[1+\left[\frac{2\Omega_R(t)}{\Delta\omega}\right]^2\right]^{1/2}} , \tag{55}$$

$$p' = \frac{\left[\frac{2\Omega_R(t)}{\Delta\omega}\right] n_0}{\left[1+\left[\frac{2\Omega_R(t)}{\Delta\omega}\right]^2\right]^{1/2}} , \tag{56}$$

and

$$p'' = -\frac{d\Omega_R(t)}{dt}\frac{2}{(\Delta\omega)^2}\frac{n_0}{\left[1+\left[\frac{2\Omega_R(t)}{\Delta\omega}\right]^2\right]^{3/2}} . \tag{57}$$

It can be readily shown that the assumptions made in obtaining (55)–(57) are valid when $\Delta\omega t_p \gg 1$ independent of the ratio $2\Omega_R(t)/\Delta\omega$. Figure 7 shows plots of the three terms, $\mathrm{Re}(p)=\frac{1}{2}p'$, $\mathrm{Im}(p)=\frac{1}{2}p''$, and n for Gaussian laser and Stokes pulses for two cases: (a) unsaturated $\Delta\omega = 10\Omega_{R,\max}$ and (b) saturated $\Delta\omega = 0.1\Omega_{R,\max}$, where $\Omega_{R,\max}$ is the Rabi frequency at the peak pump intensity. The anti-Stokes spectrum is given by

$$|E_3(\omega)|^2 \propto \left| \int dt\, e^{i\nu t}\mathcal{E}_1(t)\mathrm{Re}[p(t)] \right|^2 , \tag{58}$$

where, as before, $\nu = \omega - (2\omega_1 - \omega_2)$.

It is apparent from the form of $\mathcal{E}_1(t)$ and $\mathrm{Re}[p'(t)]$ that there is a single peak on the anti-Stokes spectrum at $\omega = 2\omega_1 - \omega_2$. In the case of weak saturation, the spectrum is given by the Fourier transform of the product of the laser field envelope squared with the Stokes field envelope. In the strong-saturation case, the spectral width will be the spectral width of the laser pulse. Thus the unsaturated anti-Stokes spectral distribution is broader than the saturated distribution. These results are in strong contrast to the square-pulse case where there are two additional components, one of which can be strong, distinctly separated from the "driven" anti-Stokes peak at $\omega = 2\omega_1 - \omega_2$. Figure 8 shows the smooth pulse spectra for the same two cases as in Fig. 7.

On resonance, when $\Delta\omega = 0$, we have an exact solution of (51)–(53) for a smoothly varying continuous pulse

$$n = n_0 \cos\left[2\int_{-\infty}^{t} dt'\,\Omega_R(t')\right] , \tag{59}$$

$$p'' = -n_0 \sin\left[2\int_{-\infty}^{t} dt'\,\Omega_R(t')\right] , \tag{60}$$

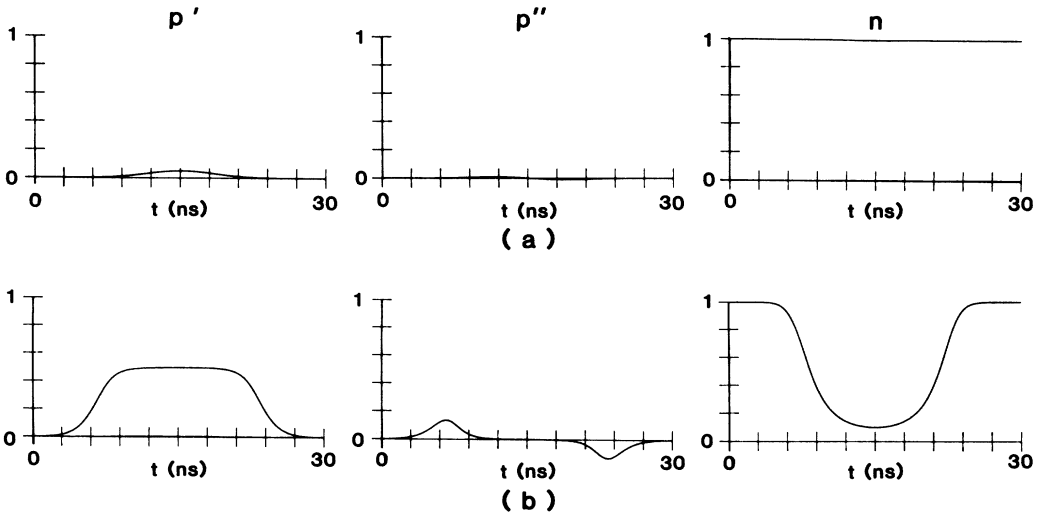

FIG. 7. Approximate analytic solutions for polarization components and population differences for Gaussian pulses when $\Delta\omega t_p \simeq 10$. (a) Weak saturation, $2\Omega_{R,\max}/\Delta\omega = 0.1$; (b) strong saturation, $2\Omega_{R,\max}/\Delta\omega = 10$.

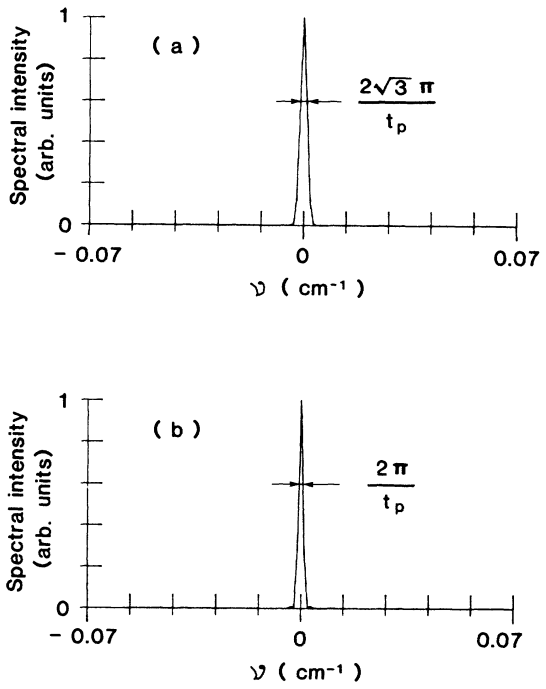

FIG. 8. Anti-Stokes spectra for synchronous Gaussian pump pulses of identical width t_p, and for $\Delta\omega t_p = 10$. (a) Weak saturation, $2\Omega_{R,\max}/\Delta\omega = 0.1$; (b) strong saturation, $2\Omega_{R,\max}/\Delta\omega = 10$.

and

$$p' = 0 \ . \tag{61}$$

This solution is expected to be a valid approximation for $\Delta\omega \neq 0$ if $p'^2 \ll n_0^2$. To test this, we use the solution (60) together with (52) to find an approximation for p' off resonance

$$p' = n_0 \Delta\omega \int_{-\infty}^{t} dt' \sin\left[2\int_{-\infty}^{t'} dt''\, \Omega_R(t'')\right] . \tag{62}$$

From this result we readily see that $p'^2 < n_0^2$ if $\Delta\omega t_p \ll 1$ for any value of the ratio $\Omega_{R,\max}/\Delta\omega$.

Instead of (58), the anti-Stokes spectrum is given by

$$|E_3(\omega)|^2 \propto \left| \int dt\, e^{i\nu t} \mathcal{E}_1(t) \mathrm{Im}[p(t)] \right|^2 . \tag{63}$$

Several features of the spectrum are apparent from the form of $\mathcal{E}_1(t)$ and $\mathrm{Im}[p(t)]$ as given by (60). For $\Omega_{R,\max} t_p \gg 1$, $\mathrm{Im}[p(t)]$ is a rapidly varying function so that we expect its Fourier transform to dominate the spectrum and, therefore, there will be spectral components extending over the range

$$2\omega_1 - \omega_2 - 2\Omega_{R,\max} < \omega < 2\omega_1 - \omega_2 + 2\Omega_{R,\max} \ .$$

Further, since a spectral component $\nu = \omega - 2\omega_1 + \omega_2$ is generated at times such that $\nu = \pm\Omega_R(t)$, we expect each spectral component $|\nu| < 2\Omega_{R,\max}$ to appear twice in the pulse, once on the leading edge, and once on the trailing edge. If these contributions are in phase, we see a peak in the spectrum; if they are out of phase we expect a minimum in spectral intensity. Further, the spectral components $|\nu| < 2\Omega_{R,\max}$ will be weak compared to the ones near $\pm 2\Omega_{R,\max}$ since the former come from the wings of the pulse and are consequently weighed less strongly by the $\mathcal{E}_1(t)$ term in (58). An example of the resulting "Airy pattern" spectrum is shown in Fig. 9. Note that the square pulse spectrum would have just two sharp peaks at $\pm 2\Omega_R$.

For $\Delta\omega t_p \simeq 1$ we solve (51)–(53) numerically in the time domain and Fourier transform to obtain the spectrum shown in Fig. 10. Note that this spectrum shows the features of both limits, namely the peak at $\omega = 2\omega_1 - \omega_l$ for $\Delta\omega t_p \gg 1$ and the "Airy pattern" spectrum for $\Delta\omega t_p \ll 1$.

The spectral shapes predicted in Figs. 9 and 10 have apparently not been observed experimentally. For them to be observed, several requirements will have to be satisfied, such as use of single-mode, short-pulse ($\lesssim 1$–2 ns long) pump beams and detection by means of either highly dispersive spectrographs or heterodyne spectroscopy; a square intensity distribution in the focal volume is also desirable for clear separation of the spectral components.

Finally, interesting diffraction phenomena can be predicted to also follow from the spectral broadening of the CARS signal at or very near resonance due to the transverse intensity variations of the pump beams, because this broadening is intensity dependent. Following are two particular cases which are noteworthy.

(1) Collinear CARS with Gaussian pump beams. If observed in the output plane of the focal volume element, this broadening depends on the radial coordinate. The spectral components with the largest shifts are found near the axis and the unshifted ones in the beam wings. Therefore, diffraction spreads out the broad spectral components in the far field more than the unshifted ones. Meanwhile, the unshifted components have a flatter intensity distribution in the focal volume, hence they undergo less diffraction than in the absence of saturation. The CARS beam should retain circular symmetry. We note that as diffraction takes the spatial Fourier transform and because the spectral content is radially dependent in the focal zone, the radial intensity distribution in the far field is, to some extent, representative of the frequency spectrum.

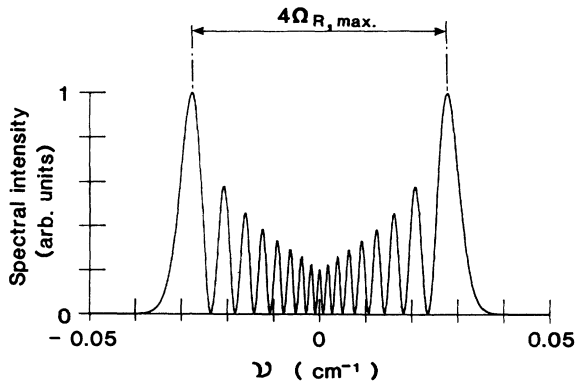

FIG. 9. Anti-Stokes spectrum for a Gaussian pulse when $\Delta\omega t_p \ll 1$ and $\Omega_{R,\max} t_p = 30$.

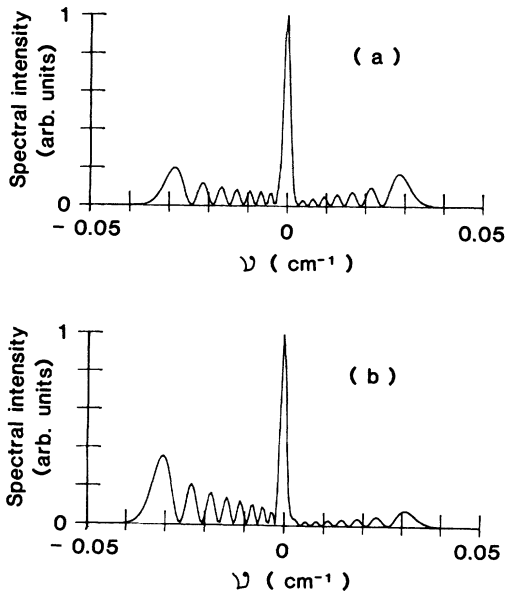

FIG. 10. Anti-Stokes spectrum for a Gaussian pulse when $\Delta\omega t_p \simeq 2$ and $\Omega_{R,\max} t_p = 30$. ($\Delta\omega = 0.001$ cm^{-1}; $I_1 = 6\times 10^{10}$ W/cm^2; $I_2 = I_1/3$.) (a) Stark effect neglected; (b) Stark effect included.

(2) Folded BOXCARS. Consider pump beams with circular cross section and with square focal intensity distribution for simplicity. In the usual geometry using weak fields and for small Raman shifts, the Stokes beam and the generated anti-Stokes beam emerge from the focal volume with their axes contained in a plane orthogonal to that defined by the ω_1 beams (Fig. 11). But we note that the two ω_1 beams interfere, causing, if strong fields are used, Stark shifts and saturation to the molecules contained in the zones of constructive interference. These zones are found in a set of parallel planes separated by the usual λ/θ, where λ is the wavelength and θ the beam crossing angle. Because the shifted radiation is created in a gratinglike structure, it is diffracted into two beams symmetrical with respect to the weak-field beams.

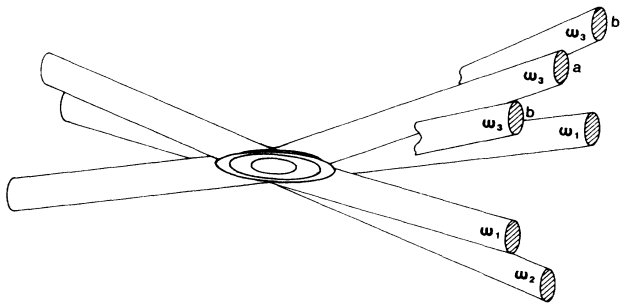

FIG. 11. Schematic of beams near focal volume in conventional folded BOXCARS geometry. Set of plane-parallel interference fringes generated at the focus by the two ω_1 pump beams is depicted; diffracted Rabi- and Stark-shifted signal beams (b) on either side of familiar unshifted CARS beam seen in the absence of saturation (a) are also shown.

III. EXPERIMENT

The preceding section has established several important points concerning the use of scanning CARS to measure quantum state population distributions in low-density gases: (i) the relative rotational line amplitudes within a vibrational manifold are little altered by saturation; (ii) the vibrational distribution is distorted by saturation and the perturbation increases with vibrational quantum number v. These predictions are now (i) compared to experimental results in order to confirm the magnitude of the pump fields required for saturation; (ii) used to correct these experimental results.

The experimental tests reported here are typical of plasma studies, namely the use of scanning CARS at moderate resolution and high-pump-beam powers. Experimentally, it is desirable to obtain the best detection sensitivity and to detect the highest possible vibrational levels. The present measurements were carried out with a multimode dye laser; the situation thus differs from the ideal situation (single frequencies ω_1 and ω_2) discussed in Sec. II and necessitates numerical simulations of saturated spectral shapes under multimode excitation.

A. Experimental setup and data analysis

Details on the experimental arrangement can be found elsewhere.[3,20] We describe here only the salient features.

1. Discharge

High purity N_2 was flowed through the discharge at pressures of 2.6 and 5.2 mbar. The gas contained $\sim 1\%$ Ar and less than 0.001% other impurities and was passed through a liquid N_2 trap for additional purification. The rotational temperature, as obtained from the CARS measurement of rotational distribution, was about 550 K in the discharge, dropping rapidly to 350 K in the post-discharge region.[20]

2. CARS setup

Frequency-doubled neodymium-doped yttrium aluminum garnet (Nd:YAG) laser radiation provided the ω_1 beam, and tunable dye laser radiation provided the ω_2 beam. The maximum pump-beam energies at the sample were in the range 30–40 mJ at ω_1 and 1–2 mJ at ω_2 and had pulse durations of 10 ns. Care was exercised to maintain these values constant during the frequency scans. The experiments were done with either collinear beams or BOXCARS, depending on experimental requirements. No suppression of nonresonant background was attempted in the experiments. A nonlinear reference signal was generated for each pulse and the CARS signal ratioed to the reference in order to reduce the effect of pump fluctuations. The reference cell and the nitrogen discharge cell were placed in series (Fig. 12).

The experiments were performed using an $f = 500$ mm focal-length achromat for focusing the input beams. Calibrated neutral density filters were placed to attenuate the pump beams between the reference cell and the discharge cell in order to further extend the range of saturation conditions. The effective focal power densities

were derived from calorimeter measurements. It was assumed that the pump-beam divergence was twice the diffraction limit. The maximum focal power densities with the 500-mm achromat thus were 30 GW/cm^2 for I_1 and 1 GW/cm^2 for I_2. The ratio of anti-Stokes powers generated in the discharge and reference cells was taken electronically, and the square root of this ratio was calculated for each laser shot. Ten consecutive measurements were taken and averaged at each point in the spectrum. This spectrum was scanned in steps of 0.015 cm^{-1}. Three adjacent spectral data points about line center were averaged in order to reduce the noise. We used this "peak" line amplitude for our measurement of the number density of quantum state population. Finally, when a filter was placed in order to attenuate the pump beams, with attenuation coefficients α_1 and α_2 (with $\alpha_1 \gtrsim \alpha_2$ because of dispersion) at frequencies ω_1 and ω_2, respectively, the spectrum was automatically multiplied by $\alpha_1 \alpha_2^{1/2}$ for normalized presentation.

3. *Spectroscopy and data analysis*

The frequency-doubled Nd:YAG pump at ω_1 is single mode, but the tunable dye laser Stokes source at ω_2 contains several adjacent cavity modes separated by $\sim$0.01 cm^{-1} over a spectral range of $\sim$0.05 cm^{-1} (FWHM). Using these lasers, the N_2 Q-branch lines at low pressure are distinct, except for $Q(0)$ and $Q(1)$ [Fig. 13(a)]. However, the lines are unresolved in the sense that their widths are smaller than the dye laser linewidth, unless very strong saturation broadens them [Fig. 13(b)]. Two limiting cases thus can be distinguished.

(a) *Low power (no and moderate saturation).* The lines are predominantly Doppler broadened, with a width of $\simeq$0.003 cm^{-1}, i.e., slightly less than the ω_2 mode spacing. Our situation is the one most commonly found in application of CARS to low-pressure gases, where the instrumental spectral resolving powers are in the range 0.05–0.3 cm^{-1}. There are two important consequences.

(i) We do not have the capability of verifying the saturated spectral shapes predicted in Sec. II, which would require the use of single-mode lasers as in recent experiments of Lucht and Farrow.[14]

(ii) Numerical simulations must be carried out of the behavior of unsaturated and moderately saturated line profiles under excitation by multimode lasers in order to understand the experimental results.

This second point requires a detailed discussion of the experimental procedure. We recall that ten shots were averaged at each point in the spectrum. We note that the scrambling caused by the inevitable shot-to-shot laser mode jitter and, when they are present, by the saturation broadening and the Stark shifting, causes the vibrational profiles to be sampled with a high degree of homogeneity, i.e., as if the Stokes laser spectrum were continuous. This conclusion remains valid even when the lines are not broadened by saturation, although their widths then are smaller than the mode spacing. Illustrative spectral shapes obtained with a multimode Stokes model are calculated below.

(b) *High power (full saturation).* This limiting case occurs when the broadening is larger than the Stokes

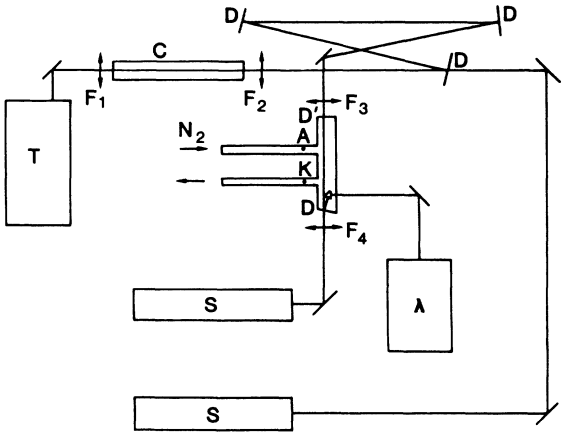

FIG. 12. Experimental setup. T, CARS laser source table; F_1–F_4, focusing achromats; C, reference cell; D, dichroic mirrors which reflect only the pump beams; D', dichroic mirror reflecting anti-Stokes beam and transmitted pump beams; A, anode; K cathode; λ, wavemeter; S, double monochromators for signal and reference isolation.

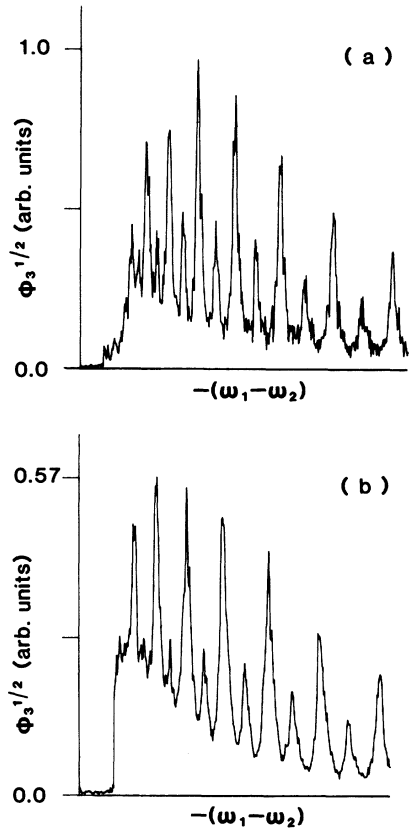

FIG. 13. Experimental CARS spectrum of the $v=3 \Leftarrow v=2$ branch of N_2 in the postdischarge region of a 2.6-mbar, 80-mA discharge using BOXCARS beam arrangement. (a) Spectrum recorded with neutral density filters giving a factor of 4 reduction in both pump beams; (b) no pump beam attenuation; note line intensity reduction and broadening.

bandwidth. This case is simple to calculate since it is then a good approximation to assume the laser to be monochromatic.

To assess these effects, numerical calculations were carried out with an extension of the techniques used to obtain the results in Sec. II. The pump pulses were 10-ns long and a nine-mode dye laser was assumed. The modes were taken to be evenly spaced by 0.01 cm^{-1} and had a Gaussian envelope, in agreement with the results of an earlier CARS study.[37] It was assumed initially that the modes had a constant amplitude but random phases chosen by a random-number generator for each simulated laser shot. Simulated CARS spectra of a single, nondegenerate [i.e., $Q(0)$] line of the $v=0$ level were obtained numerically for several values of the pump-power density product [Figs. 14(a)–14(d)]. The line was assumed to be isolated from other lines and the nonresonant background was neglected. Note that for degenerate lines ($J\neq 0$) the computation time becomes prohibitive and, as we have seen in Sec. II, the impact of the $J=0$ simplification on the line shapes is negligible. The anti-Stokes power was calculated for each point in the CARS spectrum, i.e., for each value of $\omega_1-\omega_2$, with a step size of 5×10^{-4} cm^{-1}. At low power, the dye laser mode structure is revealed as each mode passes over the Raman resonance. When the power is increased, this mode structure is blurred by the saturation and the components gradually merge into a single broad line, which is wider than the original Stokes laser profile. Note that the phase noise introduces spectral noise only when the intensity is large and the line broadened [Fig. 14(d)], so that several mode pairs simultaneously drive the density operator and interfere with each other in a random fashion.

In order to also simulate the mode amplitude fluctuations, the statistics of which are known to be exponential,[38] the same cases were calculated with allowance for random mode amplitudes in addition to the random phases [Figs. 14(e)–14(h)]. These simulations closely resemble those of Lucht and Farrow.[14] Only one calculation was done for each point in the spectrum. The spectra are seen to be very noisy under these conditions. It should be pointed out that the noise model is not strictly representative of our dye laser; the total power fluctuations (60% rms) calculated by the model were 3–5 times larger than those of the laser.

The result of the preceding calculations was then compared to simulations done with a single-mode ω_2 beam to assess the impact of the multimode character. For this

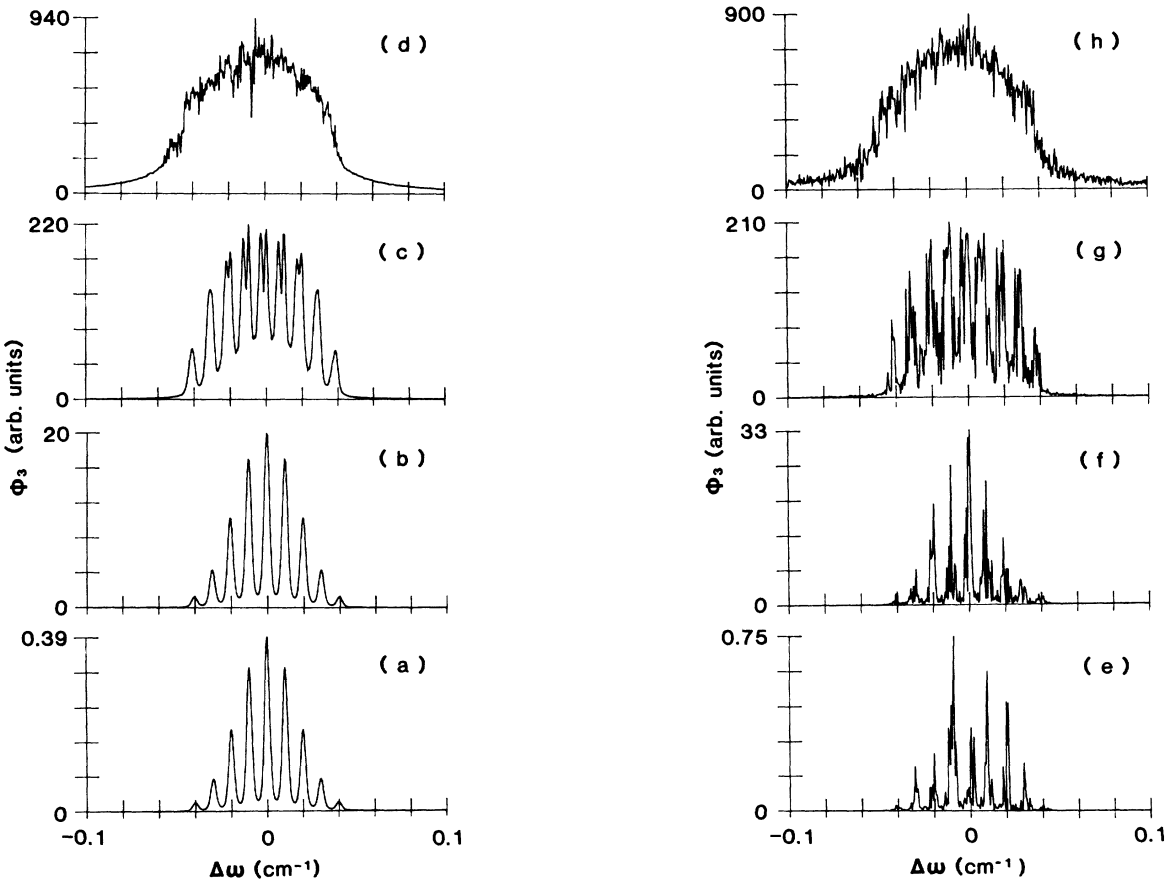

FIG. 14. Simulated CARS spectra of the N_2 $Q(0)$ line in the $v=1 \Longleftarrow v=0$ band. The line is assumed to be isolated and excited using single-mode ω_1 pump and nine-mode ω_2 dye laser; time-synchronous Gaussian pump and Stokes pulses all assumed with 10-ns duration. The Stark effect is included. Peak power densities I_1 taken for the calculations are (in GW/cm^2) (a),(e), 0.6; (b),(f), 2.4; (c),(g), 9.6; (d),(h), 38 with $I_2=I_1/3$. Calculations are for dye laser mode phase fluctuations alone (a)–(d) and with both mode phase and amplitude fluctuations (e)–(h).

comparison, we plotted the square root of the peak amplitudes of the curves shown in Figs. 14(a)–14(d) and of those obtained in a similar simulation using the same pump powers but two single-mode sources. The results are shown as a function of the square root of the product of the pump-power densities $(I_1I_2)^{1/2}$ assuming $I_1=3I_2$ (Fig. 15). The amplitudes near the peak of the multimode plot were numerically averaged over the central 0.05 cm^{-1} in order to better reflect the experimental procedure (see Sec. III A 2). For the single-mode plots, a similar average over 0.05 cm^{-1} was also taken; in addition, the variation of the true peak of the spectra is shown for comparison. We note that the three curves of Fig. 15 tend to merge for the higher powers, i.e., when the broadening becomes comparable to the multimode Stokes bandwidth or larger. The onset of saturation, however, is slower in the multimode case because the Stokes energy is spread over a spectral range larger than the CARS resonance. Also, it is seen that the two single-mode curves have different slopes at moderate saturation (i.e., below 2×10^{10} W/cm^2). If the peak spectral amplitude is plotted, a faster initial decrease is seen. The onset of saturation is practically the same for the two cases, but the error is reduced if one integrates over the spectral width. These aspects must be borne in mind when the spectra are recorded with single-mode lasers. Finally, the points calculated with mode amplitude noise [Figs. 14(e)–14(h)], which should exhibit more saturation, fall within 5–10 % of those calculated with the phase fluctuations alone. Saturation in this case is thus marginally more significant and these points have not been represented on the graph.

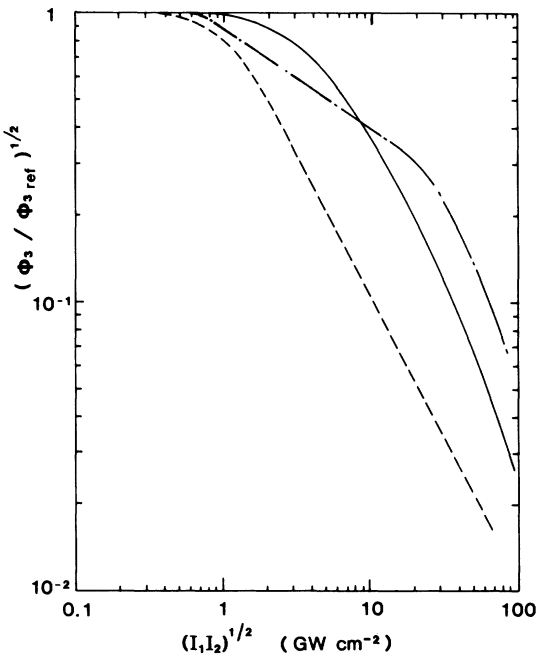

FIG. 15. Square root of calculated CARS signal vs $(I_1I_2)^{1/2}$ (solid line). To simulate the experimental method used for data acquisition, we integrate the square root of the curves shown in Fig. 14, as well as similar curves computed for complementary values of $(I_1I_2)^{1/2}$, over the central 0.05 cm^{-1}. The calculations are normalized to $(I_1^2I_2)^{1/2}$ to simulate the experimental reference ratioing cell. For comparison, a similar plot was drawn using the square-root signal calculated assuming single-mode pumps. In this case, both the central, 0.05-cm^{-1}-wide area under the square-root curves (—·—·—) and the peak (— — —) are plotted.

Strictly speaking, the influence of the Stark effect should also be studied, i.e., different values of I_1 and I_2 should be considered while keeping their product constant. However, we know from the preceding section that the main consequence of the Stark effect in the case considered here, i.e., N_2 Q-branch, is a translation of the spectra, which should have little impact on the results for the peak and integrated intensities.

B. Results

1. Rotational temperature

It is shown in Sec. II D that the rotational lines within a given vibrational manifold experience very similar distortions. As a consequence, the rotational temperature derived from CARS Q-branch contours is nearly independent of pump power. This can be verified for the saturated case by reducing the data of Figs. 13(a) and 13(b). A least-squares linear regression yields 359±8 K and 344±13 K, respectively, for the two spectra. The first four lines, $Q(0)$–$Q(3)$, were eliminated from the analysis because of their partial overlap. Similar studies of the $v=0$ and 1 bands have failed to establish, within experimental accuracy, a systematic dependence of the CARS measurement of rotational temperature on pump-power density in the range $I_1I_2=0.001$–30 (GW/cm^2)^2. This conclusion is in agreement with the predictions of Sec. III D.

2. Vibrational populations—total number densities

The measured number density difference is plotted in arbitrary units in Fig. 16 versus $(I_1I_2)^{1/2}$ for the first three vibrational quantum numbers. The data were obtained by summing the population differences in each rotational sublevel observed. Small corrections were applied for the missing contributions from undetected lines. Crossed beams (planar BOXCARS) were used. The data are seen to compare quite well with the results of numerical predictions; the calculations were carried out using the same assumptions as those of Fig. 14 (viz. nine-mode dye laser, N_2 molecular parameters, 10-ns-long pulses). The effective horizontal scale for $v=0$, however, has to be shifted by a factor of 1.8 from the theoretical one, because less saturation is seen experimentally than is calculated. This is quite probably because the simulations assume a uniform power density at the focal volume, whereas the laser beams actually have a Gaussian intensity distribution, the wings of which give an unsaturated contribution. Lucht and Farrow[14] have shown that the product I_1I_2 has to be about twice as large as in the flat profile case to obtain the same signal with Gaussian beams. Finally, Fig. 16 demonstrates that the saturation threshold decreases with vibrational quantum number, as predicted in Sec. II B. Note that the theoretical curves

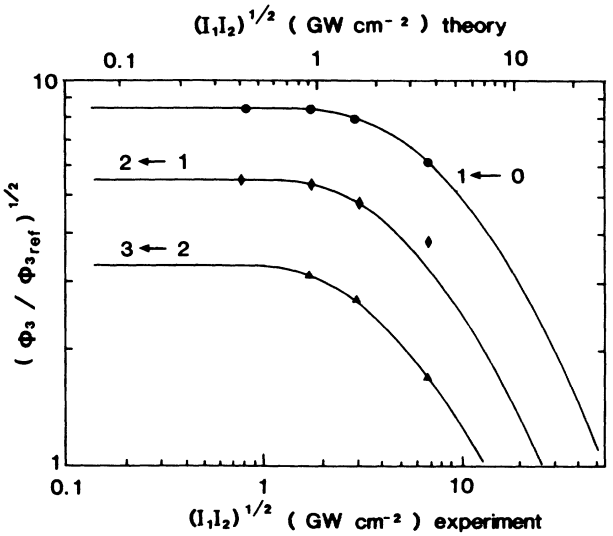

FIG. 16. Ratioed CARS signals from a 2.6-mbar discharge for $v=0,1,2$ initial states vs the product of pump-beam intensities and numerical predictions for the same transitions (solid lines). Numerical predictions are for a multimode dye laser. The theoretical curves and corresponding experimental points have been translated horizontally by a factor $\sqrt{v+1}$ and vertically by a factor of 2 for the $v=2 \Leftarrow v=1$ transition and a factor of 3 for $v=3 \Leftarrow v=2$.

corresponding to $v=1$ and 2 have been shifted exactly by the factor $\sqrt{v+1}$ with respect to the $v=0$ curve.

It is expected that Doppler broadening, which has not been included in the analysis, does not cause the discrepancy since it is small in comparison with the bandwidth of the Stokes laser modes and with the Stark and Rabi broadenings. Similar conclusions were reached by Lucht and Farrow.[14] Molecular motion, however, may have an influence on the saturation if the transit time of the molecules through the focal volume becomes comparable to or shorter than the pulse duration. For N_2, if we assume that the static (translational) temperature is equal to the rotational temperature, the transit time is approximately 100 ns at 550 K for our experimental conditions. This time is long compared with the pulse duration and should have only a very small effect on the results. We note that the situation is somewhat different for H_2 at the same temperature since the mean quadratic velocity is approximately four times larger; in other words, the saturated molecules are replaced with unsaturated ones in 20 ns. When this process is important, an inhomogeneous broadening effect is present which raises the saturation threshold. This phenomenon is not simple and shall be treated elsewhere.

Finally, assuming known temporal pump-pulse shapes and peak intensities, it becomes possible to predict the corrections which must be applied to the measurements in order to extract the exact number density differences $\Delta N(v)$ of vibrational states from the saturated values $\Delta N_{\text{sat}}(v)$, using the formula

$$\Delta N(v)=f(v)\Delta N_{\text{sat}}(v) , \tag{64}$$

where the factor $f(v)$ is derived numerically. This factor is plotted as a function of $(I_1I_2)^{1/2}$ at the bottom of Fig. 17, assuming 10-ns-duration pump pulses. Advantage was taken of the $\sqrt{v+1}$ dependence of the Rabi frequency versus $(I_1I_2)^{1/2}$ (see Sec. II B) to make the plot applicable to all vibrational states.

The top of the figure gives plots of $\sqrt{v+1}(I_1I_2)^{1/2}$ as a function of $(I_1I_2)^{1/2}$ for several values of vibrational quantum number. For known I_1 and I_2, the quantity $(I_1I_2)^{1/2}$ is first calculated. The corresponding horizontal line (a) intercepts the various v lines, giving the abscissa (b) which is to be used for each vibrational state. The resulting $f(v)$ factor is then immediately found (c) from the bottom curve. An example is given for $(I_1I_2)^{1/2}=1.3$ GW/cm^2 and $v=6$, which yields $f(v)=1.39$. Several comments should be made concerning this figure.

(1) The power density product appearing on the scales is theoretically determined assuming infinite plane waves. Experimental values producing the same levels of saturation are generally higher, by a factor which depends on the experimental arrangement and conditions (beam quality, use of BOXCARS or collinear CARS, spectral bandwidth of the Stokes, etc). Furthermore, if a molecule different from N_2 is probed, the saturation factors will be different.

(2) However, because the general features of the result are relatively insensitive to all these variables, the shape

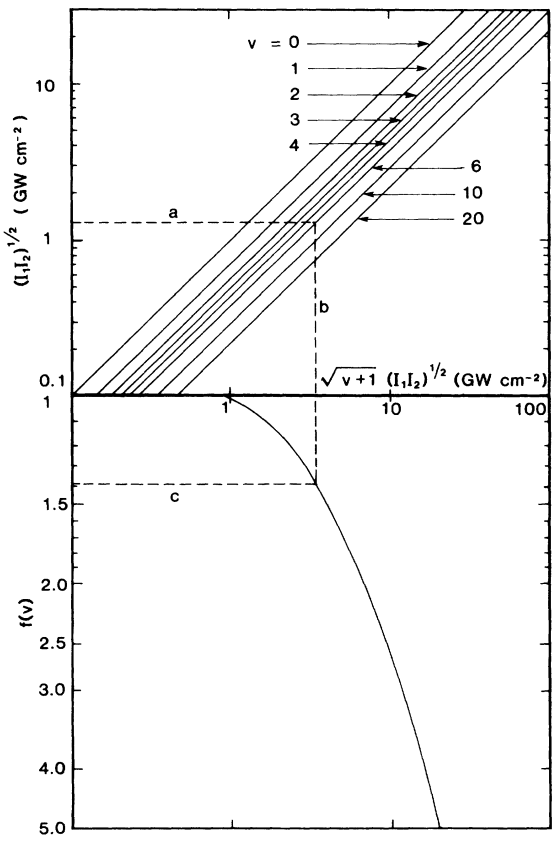

FIG. 17. Determination of the correction factor $f(v)$ in the range $0 \le v \le 20$ vs $(I_1I_2)^{1/2}$. The numerical results were calculated for N_2, assuming 10-ns-long synchronous Gaussian pulses, monochromatic ω_1 and 0.05 cm^{-1} bandwidth, nine-mode ω_2 beams (same conditions as Fig. 15).

of the curve should remain approximately valid over a fairly wide range of experimental conditions, assuming the parameter $(I_1 I_2)^{1/2}$ is suitably adjusted. With this provision, we feel that the correction factor given by the figure may be used for resolutions varying from single mode to a few 10^{-1} cm^{-1}, diffraction-limited or multiple transverse mode beams, collinear CARS or BOXCARS, and any diatomic molecule.

(3) In order to determine the $(I_1 I_2)^{1/2}$ parameter which is suitable for a particular experiment, it is recommended that $f(v)$ be carefully determined experimentally for one or a few low-vibrational states. This can be done by recording their line amplitudes under two distinct conditions: (a) the nominal pump powers at which all molecular states of interest are to be studied; generally, this power is the highest possible in order to achieve the best detection sensitivity and is assumed to be kept constant for the entire study; (b) the lowest possible power still permitting good detection sensitivity and absence of saturation for low-vibrational states. Using the $f(v)$ value(s) thus obtained, Fig. 17 then can be used to find the pertinent $(I_1 I_2)^{1/2}$ from which $f(v)$ will be derived for all other vibrational quantum numbers. The higher the vibrational state(s) used in the first step, the more accurate the final coefficients. Finally, note that the curve has been limited to $f(v) \leq 5$, beyond which there are strong saturation and large spectral widths and shifts; therefore, the validity of experimental data becomes questionable.

IV. CONCLUSION

We have calculated and experimentally observed the consequences of vibrational saturation and Stark shifting in rovibrational CARS spectra; the effects are quite significant. They are, however, virtually independent of rotational quantum number J in any given vibrational manifold, which facilitates the measurement of rotational temperature. Saturation increases monotonically as a function of the vibrational quantum number v. Large effects (up to 100%) have been seen experimentally in a typical CARS measurement of vibrational state densities in a low-pressure nitrogen glow discharge. The correction factors necessary to derive the populations from saturated measurements have been calculated and experimentally verified.

High-lying vibrational states are usually detected under conditions of relatively strong saturation because they require use of the highest available pump powers and because achieving good spatial resolution necessitates tight focusing. Data correction is therefore necessary in most low-pressure CARS work and the chart given in Fig. 17 permits this correction to be calculated for N_2 under experimental conditions similar to those used here (no collisions, single-mode ω_1 pump and multimode, 0.05 cm^{-1} bandwidth ω_2 pump, and either BOXCARS or collinear beams). In addition, Fig. 17 should be applicable to a wider range of experimental conditions covering, e.g., other molecules, or use of single-mode pump lasers. However, its application should be restricted to intermediate saturation power levels; above these powers, differences may appear, in particular when the Stark effect is more pronounced than in N_2. Because of the observed sensitivity to saturation, many previous CARS low-pressure measurements probably will have to be revisited using correction techniques.

Effects not previously seen in conventional, off-electronic resonance CARS include (a) spectral broadening of the CARS signal caused by the dynamic population redistribution; (b) altered divergence of the saturated spectral components present in the CARS signal beam compared with the unsaturated case, viz. increased divergence of the shifted components and reduced divergence of the unshifted components. In folded BOXCARS, new, well-defined signal beams appear.

Collisional damping has not been considered here. Our analysis is therefore strictly valid only for pressures below 10 mbar. We have recently seen evidence of saturation in multiplex CARS in flames under higher pressure conditions; appreciable temperature measurement errors were found to occur. A report of vibrational saturation in multiplex CARS was also recently published and a rate equation model of the saturation was presented.[15] While this approach of the problem may be valid at moderate pump powers, we feel that a treatment of the multiplex CARS case based on our model with the inclusion of damping or, equivalently, the analysis of Lucht and Farrow,[14] is necessary.

ACKNOWLEDGMENTS

The authors thank R. Lucht and R. Farrow for kindly providing a report of their work on saturation prior to publication. This work was supported in part by Direction des Recherches et Etudes Techniques (DRET). The Lincoln Laboratory portion of this work was sponsored in part by the U.S. Navy for the Strategic Defense Initiative Organization and in part by the Department of the Air Force.

[1]D. N. Kozlov, V. V. Smirnov, and V. I. Fabelinskii, Dokl. Akad. Nauk. SSSR **246**, 304 (1979) [Sov. Phys.—Dokl. **24**, 369 (1979)].

[2]A. Owyoung and P. Esherick, Opt. Lett. **5**, 421 (1980).

[3]S. A. J. Druet and J. P. E. Taran, Prog. Quant. Electron. **7**, 1 (1981).

[4]M. Duncan, P. Oesterlin, F. Konig, and R. L. Byer, Chem. Phys. Lett. **80**, 253 (1981).

[5]C. Mavroyannis, Can. J. Phys. **59**, 1917 (1981); C. Mavroyannis, K. Woloschuk, D. A. Hutchinson, and C. Downie, *ibid.* **60**, 245 (1982).

[6]F. Ouellette and M. M. Denariez-Roberge, Can. J. Phys. **60**, 877 (1982); **60**, 1477 (1982).

[7]A. D. Wilson-Gordon, R. Klimovsky-Barid, and H. Friedmann, Phys. Rev. A **25**, 1580 (1982).

[8]A. D. Wilson-Gordon and H. Friedmann, Chem. Phys. Lett.

89, 273 (1982).
[9]H. Weil and P. W. Schreiber, Appl. Opt. **21**, 941 (1982).
[10]G. S. Agarwal and Surendra Singh, Phys. Rev. A **25**, 3196 (1982).
[11]A. M. Brodnikovsky, V. N. Zadkov, M. G. Karimov, and N. I. Koroteev, Opt. Spektrosk. **54**, 385 (1983) [Opt. Spectrosc. (USSR) **54**, 227 (1983)].
[12]V. N. Zadkhov and N. Koroteev, Chem. Phys. Lett. **105**, 108 (1984).
[13]A. M. Levine, N. Chencinsky, W. M. Schreiber, A. N. Weiszmann, and Y. Prior, Phys. Rev. A **35**, 2550 (1987).
[14]R. P. Lucht and R. L. Farrow, J. Opt. Soc. Am. B **5**, 1243 (1988).
[15]A. Gierulski, M. Noda, T. Yamamoto, G. Marowski, and A. Slenczka, Opt. Lett. **12**, 608 (1987).
[16]L. A. Rahn, R. L. Farrow, M. L. Koszykowski, and P. L. Mattern, Phys. Rev. Lett. **45**, 620 (1980).
[17]R. L. Farrow and L. A. Rahn, Phys. Rev. Lett. **48**, 395 (1982).
[18]B. Y. Kryzhanovskii and A. O. Melikyan, Kvant. Electron. (Moscow) **13**, 734 (1986) [Sov. J. Quantum Electron. **16**, 477 (1986)].
[19]Yu A. Il'inskii and V. D Taranukhin, Kvant. Electron. (Moscow) **1**, 401 (1974) [Sov. J. Quantum Electron. **4**, 224 (1974)].
[20]B. Massabieau, G. Gousset, M. Lefebvre, and M. Péalat, J. Phys. (Paris) **48**, 1939 (1987).
[21]G. Placzek, in *Handbüch der Radiologie,* edited by E. Marx (Academische Verlagsgesellschaft, Leipzig, 1934).
[22]E. G. Garmire, F. Pandarese, and C. H. Townes, Phys. Rev. Lett. **11**, 160 (1963).
[23]J. A. Giordmaine and W. Kaiser, Phys. Rev. **144**, 676 (1966); M. Maier, W. Kaiser, and J. A. Giordmaine, *ibid.* **177**, 580 (1969).
[24]V. S. Butylkin, A. E. Kaplan, and Yu G. Khronopoulo, Zh. Eksp. Teor. Fiz. **59**, 921 (1970) [Sov. Phys.—JETP **32**, 501 (1971)].
[25]M. Takatsuji, Phys. Rev. A **11**, 619 (1975).
[26]D. Grischkowsky, M. M. T. Loy, and P. Liao, Phys. Rev. A **12**, 2514 (1975).
[27]A. Schnezle and R. G. Brewer, Phys. Rev. **43**, 455 (1978).
[28]H. Friedmann and A. D. Wilson-Gordon, Opt. Commun. **24**, 5 (1978).
[29]H. Friedmann and A. D. Wilson-Gordon, Opt. Commun. **26**, 193 (1978).
[30]L. Allen and J. Eberly, *Optical Resonance and Two-Level Atoms* (Wiley, New York, 1975).
[31]V. S. Butylkin, A. E. Kaplan, Yu. G. Khronopoulo, and E. I. Yakubovich, *Resonant Nonlinear Interaction of Light with Matter* (Nauka, Moscow, 1977).
[32]R. P. Feynman, F. L. Vernon, and R. W. Hellwarth, J. Appl. Phys. **28**, 49 (1957).
[33]D. Grischkowsky, Phys. Rev. Lett. **24**, 866 (1970).
[34]C. Cohen-Tannoudji, B. Din, and F. Laloë, *Mécanique Quantique* (Hermann, Paris, 1973), Vol. 1 [*Quantum Mechanics* (Wiley, New York, 1977), Vol. 1].
[35]K. P. Huber and G. Herzberg, *Constants of Diatomic Molecules,* Vol. 4 of *Molecular Spectra and Molecular Structure* (Van Nostrand, New York, 1979).
[36]M. A. Morrison and P. J. Hay, J. Chem. Phys. **70**, 4034 (1979).
[37]F. Moya, ONERA Technical Report No. 1975-13, 1976 (unpublished) [European Space Agency English technical translation ESATT 331, 1976 (unpublished)].
[38]V. M. Baev, G. Gaida, H. Schröder, and P. E. Toschek, Opt. Commun. **38**, 309 (1981).